Hindawi
Journal of Electrical and Computer Engineering
Volume 2024, Article ID 3035524, 16 pages
https://doi.org/10.1155/2024/3035524

Research Article

Design of PV, Battery, and Supercapacitor-Based Bidirectional DC-DC Converter Using Fuzzy Logic Controller for HESS in DC Microgrid

Senthil Kumar Ramu,[1] **Indragandhi Vairavasundaram**,[2] **Belqasem Aljafari**,[3] **and Tareq Kareri**[3]

[1]*School of Electrical Engineering, Vellore Institute of Technology, Chennai 600127, Tamil Nadu, India*
[2]*School of Electrical Engineering, Vellore Institute of Technology, Vellore 632014, Tamil Nadu, India*
[3]*Department of Electrical Engineering, College of Engineering, Najran University, Najran 11001, Saudi Arabia*

Correspondence should be addressed to Indragandhi Vairavasundaram; indragandhi.v@vit.ac.in

Received 13 July 2023; Revised 23 February 2024; Accepted 2 March 2024; Published 8 March 2024

Academic Editor: R. Palanisamy

Renewable energy sources (RES) are becoming more popular globally as a reaction to critical energy concerns. Modern energy management technologies are used to maximize their efficiency while preserving the reliability of the grid. A hybrid energy storage system (HESS) connects to the DC microgrid through the bidirectional converter, allowing energy to be transferred among the battery and supercapacitor (SC). In this paper, a fuzzy logic control (FLC) technique is developed for PV-based DC microgrid systems that use both batteries and SCs. The proposed method uses the unbalanced energy from the battery pack to enhance the overall effectiveness of the HESS. The FLC approach is performed to validate under conditions of variable irradiance using MATLAB Simulink. When sudden changes in irradiance occur, the proposed FLC brings the voltage back to the desired level in terms of transient response like 33 ms settling times and 19% overshoot values. The results exhibit that the proposed method is more efficient in terms of time response, power output, increasing battery life, and ensuring a continuous supply of the PV system.

1. Introduction

Renewable energy installation has grown in popularity over the last few decades, mainly due to the need to reduce reliance on fossil fuels and coal and reduce pollutant emissions. Expanding renewable energy is the primary method for meeting the climate targets [1], according to IRENA (International Renewable Energy Agency). Worldwide renewable energy capacity attained 3.8 TW in 2022 with installations of 280 GW, the most significant year rise ever. In addition, wind (563 GW), hydro (1173 GW), and solar (487 GW) accounted for the majority of the world's renewable power capacity, which stood at 2351 GW by the end of 2019 [2]. Besides, wind and solar technologies accounted for eighty per cent of the new capacity installed in 2018. However, its production and reliability are quickly impacted by irregular operating circumstances, such as variations in irradiance, moisture, and partial shading consequences [3]. The production of RESs and the demand for loads are sporadic in real-world scenarios. An energy storage system (ESS) can help to improve management by providing frequency, increasing power factor, and decreasing system fluctuations [4].

Many recent studies have focused on the capacity configuration of ESS with various RES, which are broadly classified into two distinct groups: technical and economical [5]. The layout of storage capacity for energy based on economic variables typically takes into account revenue and various cost factors during the power plant's lifecycle [6], as well as the total expense of operation of the optical storage facility [7].

The battery energy storage system (BESS) is the simplest ESS to design. The BESS is substantially less affected by

environmental changes [8]. HESS is typically used to handle such problems. HESS has a benefit over a single ESS in that it can efficiently use the characteristics of many energy storage technologies. One of the standard HESS setups is the pairing of battery and SC [9]. The modest average power demand is made up by using batteries with high energy densities.

Moreover, its lifespan is reduced if exposed to repeated transient power oscillations. With reduced strain on the BESS, this grouping can successfully and effectively resolve the variable power variations. Therefore, an effective control approach is crucial for the HESS to operate at its best under varied load demands [10, 11]. In [12], a HESS combining batteries and supercapacitors is presented using sophisticated electrothermal modelling. Multiple-Input Bidirectional Converters (MIBC) perform significantly better at energy trade-offs between input sources. Significant advantages of the MIBC include improved energy trading across input sources, a modular framework design, and cheaper converter costs [13]. A few input topologies have been described for fusing several sources with various features. Several ESSs are linked to a three-transformer utilizing full-bridge circuit on each end. Eight switches are needed for a battery-SC-based HESS in DC microgrid, which may impact total efficiency. An independent multiport DC-DC converter known as a battery-SC can control power from many sources and deliver it directly to an individual component [14, 15]. While sources had been swapped out for ESS, the power transfer among the inputs and the ESS was not examined. Although isolated converters could manage various voltage levels and assure stability by isolation, and controlling energy through several sources is more complicated.

Song et al. [16] present a semiactive battery/SC HESS that includes a unidirectional DC/DC converter to reduce system costs while boosting system efficiency for electric vehicle (EV) applications. To offer frequency provision for off-grid systems, Bahloul and Khadem [17] expand on a HESS that utilizes a superconductive electromagnetic storage-battery principle. In this arrangement, the battery's Depth of Discharge (DOD) variation is significantly reduced by the Low Pass Filter (LPF)-based power-sharing mechanism, resulting in a 32% increase in battery life over the ordinary model. The algorithms that control power flow and the connections between the various storage devices in the hybrid solution determine how much power can be shared. An optimised energy preservation and distribution system model over uncertain of the power production issue based on an improved gravitation search algorithm (IGSA) is presented in [18].

According to Bazargan et al. [19], the input impedance and internal voltage changes in the battery impact the converter attached to the battery part. This investigation shows that changes in internal features affect both the battery reaction time and the DC voltage link regeneration time during one load shift. The stability problems with the cascaded DC-DC converter are represented in [20]. The variations in battery SoC and the capacity of various energy storage systems can result in control stability issues.

The adaptive filter-Based DC microgrid operation was presented in [21]. It prioritizes stable and smooth performance, simultaneously resolving concerns related to storage device deterioration and safety. In [22], it is proposed that, the optimize cost and power reserve of a hybrid energy system in a stand-alone DC microgrid. The battery meets the low variation element of load demand and renewable energy production, while the SC delivers the high variation element. To optimize the cost of reduced PV energy and SC investment, a cost-effective transient energy sharing scheme between both short- and long-term energy supplies is proposed in [23], along with its parameters design technique.

The sliding mode control (SMC) for the HESS was introduced by Kollimalla et al. [24]. In the study, the selection of the detailed controller settings and SC sizing are covered. The behaviour of the system's slope is indifferent and has model errors. Rout et al. [25] presented a two-state proportion limit control for HESS implementation in an independent DC electric grid. The suggested method supports decreasing the BESS's current rate. The decentralized control strategy for HESS is proposed in [26]. This approach effectively maintains the battery's SOC at a high level for an extended period. However, the abrupt shift in charge/discharge current rate might shorten the lifespan of the battery.

Yi et al. [27] established a unique command of power management of PV for grid-connected and stand-alone operations. Under all operational circumstances, the battery regulates the energy of the microgrid in the specified control plan. It causes an increase in the stress of battery, total cost, and battery life. The interleaved converter circuit features a complex control scheme that needs eight switches [28]. For managing energy demand in battery-based DC microgrids, the fuzzy logic controller (FLC) is described [29]. High peak charging and discharging rates shorten a battery's lifespan; however, they are necessary to control the energy demand. Thus, an FLC for battery-ultracapacitor-based microgrids is proposed in this research to address this problem. The FLC manages the power balance for HESS and DC connections and regulates the DC bus voltage by controlling the SC. The existing topologies are focused on individual components of ESS. This paper proposes the integration of HESS through a bidirectional converter (BC) with FLC, which provides the solution for optimal load balance in PV-based microgrid systems. Figure 1 depicts the HESS design with a FLC-based BC arrangement. The main contributions of this article are illustrated as follows:

(i) Implementation of HESS-based BC with FLC integration of PV/Battery/SC

(ii) For fixed and variable irradiance and temperature circumstances, energy management performance for a BC utilizing HESS is presented

(iii) The proposed approach optimally controls the ESS charging/discharging process

(iv) When related to existing schemes, the proposed approach improves the load balancing and better time domain characteristics

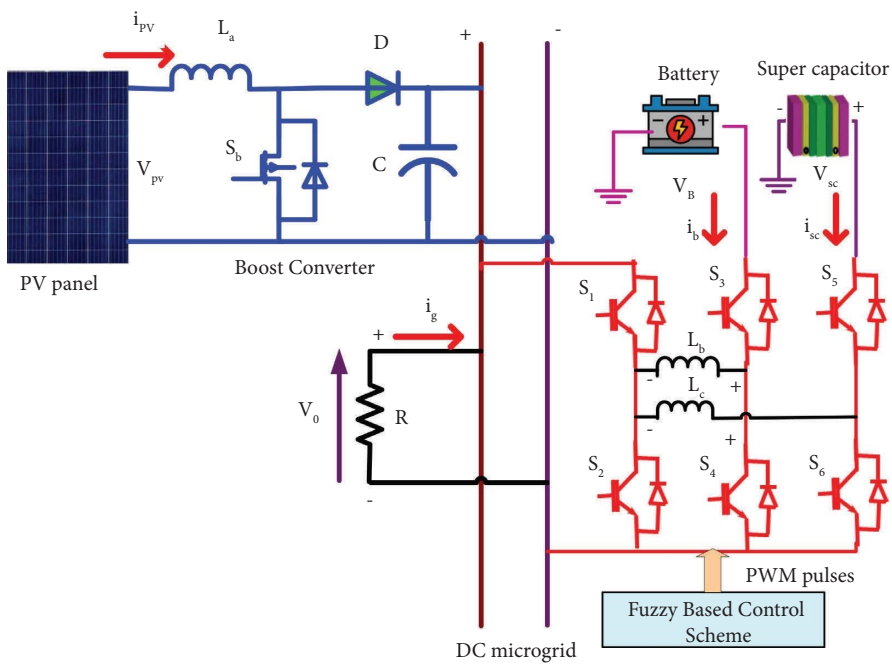

Figure 1: Block diagram of proposed BC for DC microgrid.

This article is written as follows: Section 2 discusses the BC electrical grid layout. Section 3 focuses on the modelling of battery and SC. Section 4 deals with the controller design for HESS. Section 5 explains the results obtained from the observations. Section 6 discusses the proposed FLC with the existing PI controller. Section 7 summarizes the study outcomes and future directions.

2. Mathematical Modeling of Battery and SC

This section illustrates the electrical behaviours and features of the battery and SC in the HESS.

2.1. Battery. A simplified electrically connected battery model is constructed using resistances, voltage sources, and capacitors and is represented in Figure 2.

Equations (1) and (2) are found by applying KCL to the circuit [30].

$$\dot{V_1}(t) = -\frac{1}{R_1C_1}V_1(t) + \frac{I(t)}{C_1}, \tag{1}$$

$$\dot{V_2}(t) = -\frac{1}{R_2C_2}V_2(t) + \frac{I(t)}{C_2}. \tag{2}$$

The derivatives of the voltage V_1 and V_2 are represented as $\dot{V_1}(t)$ and $\dot{V_2}(t)$.

Equation (3) is found by applying KVL to the circuit.

$$V_T(t) = V_{OC}(Z(t)) - V_1(t) - V_2(t) - R_sI_t, \tag{3}$$

where V_{OC} is the internal open circuit voltage, V_1 and V_2 are the voltage drops across the combination in parallel, and R_s is the internal resistance.

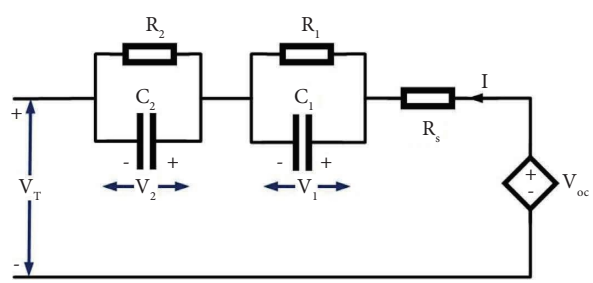

Figure 2: Equivalent circuit of battery.

State space model can now be described by the following generic equations [31]:

$$\dot{X}(t) = Ax(t) + Bu(t), \tag{4}$$

$$y(t) = Cx(t) + Du(t), \tag{5}$$

where state variable $x(t) = [V_1(t)\ \ V_2(t)]$; input variable $u(t) = I(t)$; output variable $y(t) = V_T(t)$; $A = \text{diag}[-1/R_1C_1\ \ -1/R_2C_2]$; $C = [-1\ -1]$; $D = [-R_s]$; and $B = [1/C_1\ 1/C_2]^T$

2.2. Supercapacitor. Figure 3 illustrates a mathematical example of a SC made of capacitors and resistors. The terminal voltage (U) can be written as

$$U = iR_s + V_c. \tag{6}$$

The current through the SC can be represented as [32]

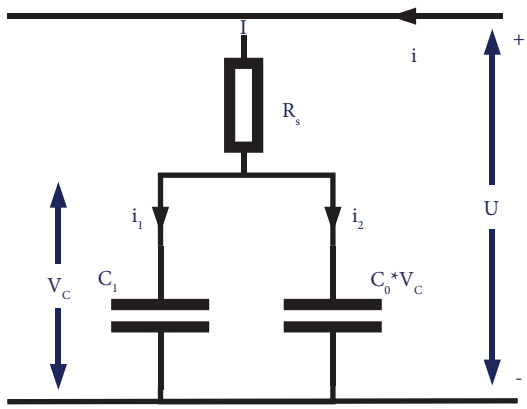

Figure 3: Equivalent circuit of SC.

$$\begin{aligned} i &= i_1 + i_2 \\ &= C\frac{\mathrm{d}Vc}{\mathrm{d}t} + C_0 V_c \frac{\mathrm{d}Vc}{\mathrm{d}t}, \end{aligned} \tag{7}$$

where R_s is the internal resistance, and i_1 and i_2 are the dispersed currents in ampere (A) passing through the corresponding capacitors with capacitance values of C and $C_0 V_c$.

The state equation can be written as [30]

$$\frac{\mathrm{d}Vc}{\mathrm{d}t} = \frac{i}{C + C_0 V_c}. \tag{8}$$

2.3. Integration of Battery and SC. SC and battery HESS has been proposed in recent years to raise the efficiency and extend the HESS lifespan [33]. The SC has a substantial lifespan and a notable power density but a poor energy density. To control the operation of HESS, the proposed work will look at the HESS architecture of battery and SC. The BC can incorporate the battery and SC as HESS to alleviate the power imbalance between PV power and load demand. In addition to meeting the demands of the network operator, the proposed system also allows for the optimal functioning of a HESS integrated into a PV plant. Except for a small amount from the SC to lessen battery stress, the lead-acid pack will be the primary storage technology utilized in the peak power saving assistance, which requires the HESS to exchange power constantly for a few hours. Long-term energy storage and rapid reaction to abrupt load changes are made possible by the HESS, which combines the battery's high energy density with the substantial power density of SC.

3. Operation of Proposed Converter

BC with two inputs is shown in Figure 4, along with a detailed explanation of the various operating modes [34]. The improved principle of the converter is discussed below. It consists of three switch limbs. Legs 2 and 3 are wired to the battery voltage (V_B) and SC voltage elements, respectively, while Leg 1 is wired to a microgrid voltage module (V_{DC}). In this configuration, the battery voltage is higher than the SC voltage but lower than the DC utility grid. The sections that follow discuss the various methods of operation.

3.1. Mode 1-Discharging Sequence. The microgrid voltage drops when the load surpasses PV generating capacity or when PV power is lowered due to decreased solar irradiation [35]. Throughout this time, the HESS should provide enough electricity. The converter's functioning can be divided into three time periods, as indicated in Figure 5. Switch pairs that act in tandem include S_1/S_2, S_3/S_4, and S_5/S_6. The switch pairs S_2/S_5 and S_1/S_6 always change together in this mode, with complimentary gating pulses.

The output voltages are achieved by balancing the inductors in volts per second.

$$\begin{aligned} V_{\mathrm{dc}} &= \frac{d_s}{1 - d_s} V_s, \\ V_{\mathrm{dc}} &= \frac{d_b}{1 - d_b} V_b, \end{aligned} \tag{9}$$

where d_s and d_b are the converter's duty cycle of SC and battery. Here, V_b is larger than V_s, duty cycle d_b must always be lower than d_s. As a consequence, by adjusting d_s and d_b, the DC microgrid's power supply from the battery and SC may be independently managed.

3.2. Mode 2-Charging Sequence. While PV-induced power exceeds the amount needed by demand, additional power exists in the DC microgrid. Sufficient power will be utilized for charging the battery as well as the SC. As a result, in this mode, power is transferred from the DC microgrid to the HESS. The converter in this mode is divided into three time periods, as indicated in Figure 6. Switch pairs for S_1 and S_6 are switched simultaneously. Switch pairs S_2 and S_5 are also triggered instantaneously, with pulses complementing S_1 and S_6. Additionally gated similarly are switches S_4 and S_3.

The inductor currents (i_b and i_c) fall exponentially in a negative way with slopes of V_{dc}/L_b and V_{dc}/L_S, respectively, at t_0 when the switches S_4, S_1, and S_6 are triggered. The inductors (L_b and L_S) retain energy at this time until instant t_1. The S_2's body diode allows the inductor current i_b to flow freely. ZVS applies a triggering pulse over dead periods to switch on S_1, S_4, and S_6.

$$\begin{aligned} V_s &= \frac{d_s}{1 - d_s} V_{\mathrm{dc}}, \\ V_B &= \frac{d_s}{1 - d_b} V_{\mathrm{dc}}. \end{aligned} \tag{10}$$

3.3. HESS Mode. A SC is HESS's conversion efficiency unit. Its fast self-discharging activity prevents it from serving as a battery for extended periods [34]. For the element ESSs to function effectively in microgrid systems, they should have adequate stored energy. For the HESS to function correctly,

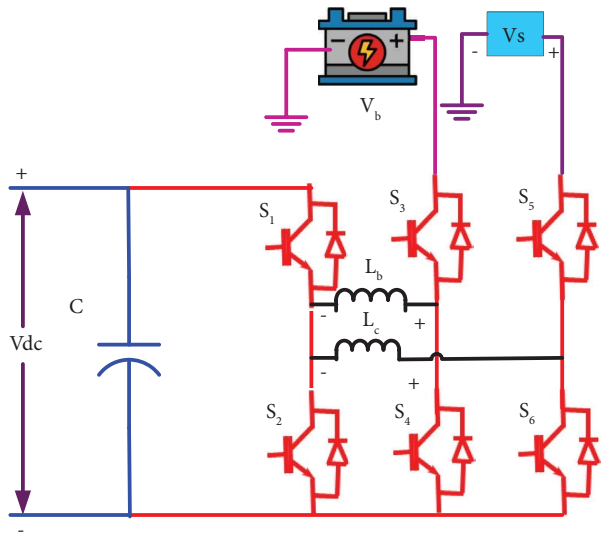

Figure 4: Proposed BC topology with HESS.

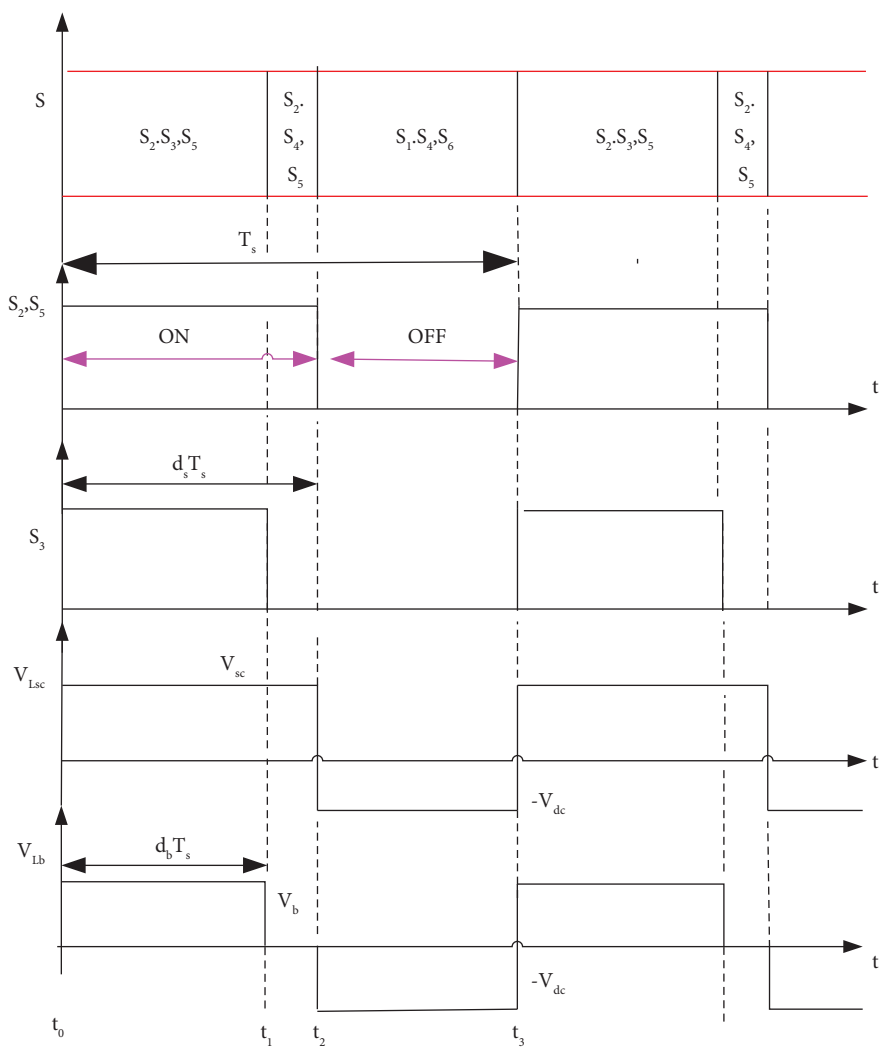

Figure 5: Waveforms of discharging sequence.

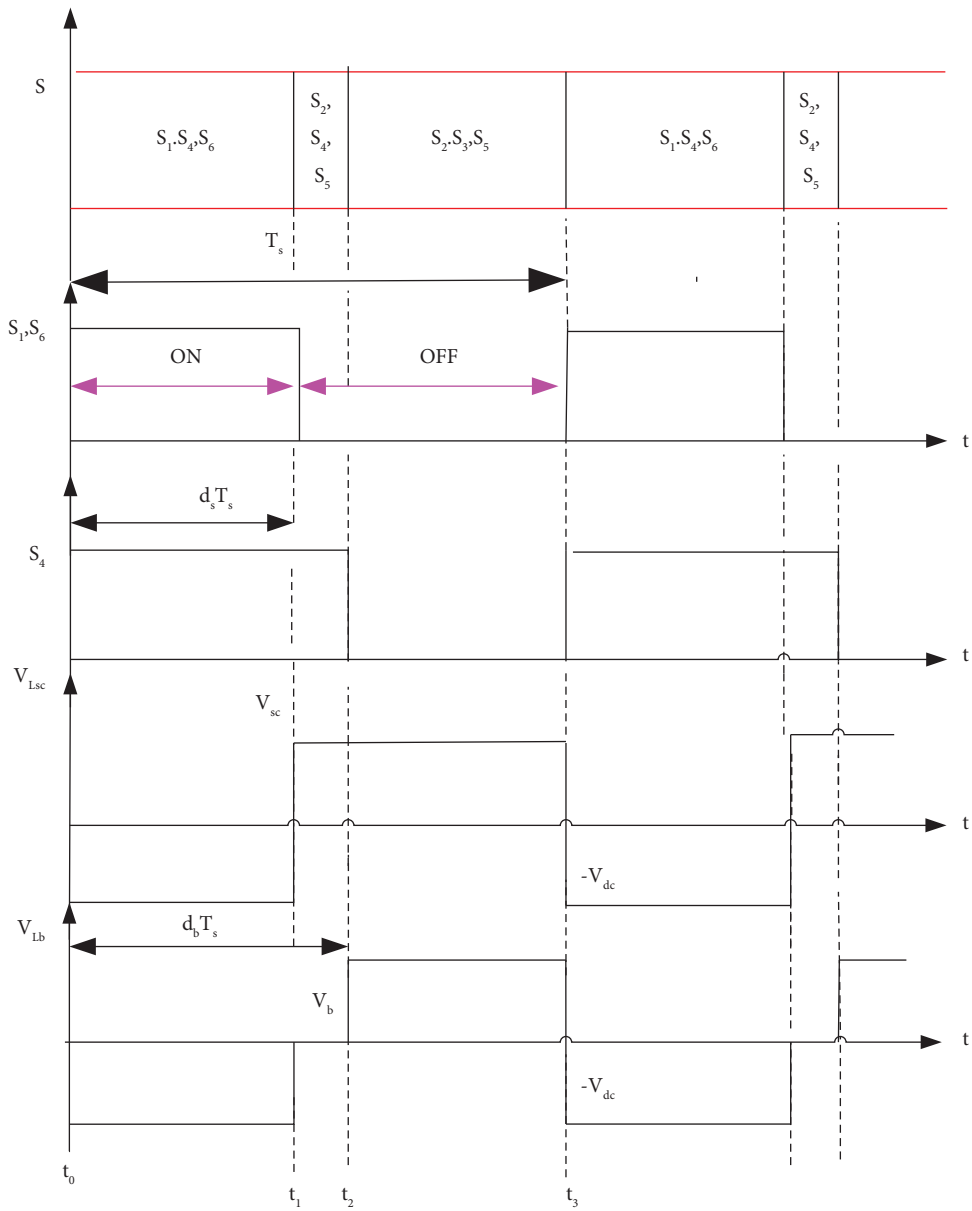

Figure 6: Waveforms of charging sequence.

the SC should be charged within permitted values. The circuit configuration for this mode is shown in Figure 7. It effectively isolates the DC microgrid when the SC is charged since the switches S_1 and S_2 are passive. Switch S6 is not working since the switch S_5 is always on during this mode. The switch S_3 is subjected to the duty cycle (d). Using the "d" parameter, the user may modify the power balance between the battery and SC.

$$V_s = d.V_b. \tag{11}$$

In addition, power can go from the SC to the battery owing to the switch S_3's complementing function. This action shows that switch S_4 is in boost mode. The process is comparable to the one previously discussed.

4. Design of Controllers in HESS

4.1. Conventional PI Controller. Figure 8 depicts the control system block schematic for the traditional PI. The traditional control strategy will add a controller that offers better closed-loop performance. In all approaches, the nominal DC-associated voltage (V_{DC}) and a reference voltage (V_{DC}, ref) are compared, and the error is provided to a controller that creates the entire current in the process [36]. The total current in the existing strategy is separated into frequency components using a low-pass filter, and these components are then supplied as line current to the battery and SC loop, respectively. The SC current reference in the traditional control scheme includes both high-frequency and battery error elements. The standard control strategy disregards

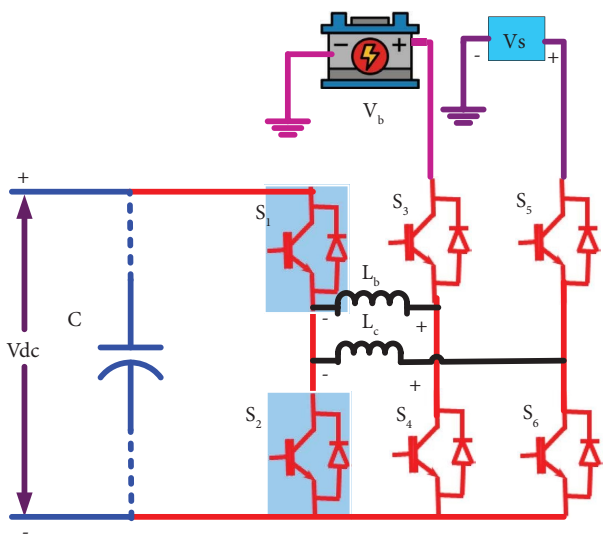

Figure 7: HESS mode of operation.

battery current faults brought on by the battery controller. The power balance equation is represented as follows:

$$P_{dc}(t) - P_R(t) = P_b(t) + P_{sc}(t) = P_{ss(t)} + P_{ts(t)}, \quad (12)$$

where $P_{sc}(t)$, $P_R(t)$, $P_{dc}(t)$, $P_b(t)$, and are power of SC, RES, DC grid, battery, and SC, respectively. $P_{ss(t)}$, and $P_{ts(t)}$ are steady state and transient component. By charging/discharging, the HESS keeps the grid voltage within set bounds [37]. The total power from the battery and SC is shown as

$$P_b(t) + P_{sc}(t) = P_{ss(t)} + P_{ts(t)} = V_{dc}.i_t. \quad (13)$$

The overall current demand to manage the DC link voltage is shown below

$$i_t = \frac{P_{ss}(t) + P_{ts}(t)}{Vdc(t)} = i_{ss}(t) + i_{ts}(t). \quad (14)$$

The total current demand is determined by the voltage control loop in the manner described below

$$i_t = i_{ss}(t) + i_{ts}(t) + K_{p.Ve} + K_i \int V_e.\,dt. \quad (15)$$

Although the charging and draining of the battery/SC share the same transmission element, the complementary functioning of the switch makes the controller adequate. When building the linear model, the HESS discharge mode is considered. The outer loop is constructed around the eventual SC due to its quick response.

4.2. Proposed Fuzzy Logic Controller. An FLC's basic concept is to leverage a human expert skills and knowledge to develop a controller for controlling an enrollment procedure where the input link is defined by assembling fuzzy rules using linguistic parameters rather than a sophisticated dynamic system [38]. Two inputs and one output are included in the FLC's architecture. The modulating signal is taken as the output, while the error and change in error are reserved as the input. FLC mostly adheres to the four essential processes, including:

(i) Input is transformed into fuzzy variables by an analogue fuzzifier
(ii) It also stores fuzzy rules
(iii) It makes inferences and applies related rules
(iv) A fuzzified then turns the fuzzy variables back into the real targets

The HESS's inference system determines the HESS's charging and discharging rates. The primary function of the EMS in this control approach is to offer optimal power flow, improved efficiency, and increased system dependability. The proposed controller for the energy management system with BC is shown in Figure 9. In this instance, the inaccuracy serves as a metaphor for a mismatch between supply and demand. The battery's charge level is determined by its State of Charge (SoC). The FLC receives these inputs, and the duty cycle is acquired as an output. The membership function of output is represented in Figure 8. This study analyses the reference current in the system and uses the FLC to modify the DC link voltage.

The variation between a reference voltage, the bus bar voltage, and the battery charge level are fuzzy input variables. This study analyses the reference current in the system and adjusts the DC link voltage using the FLC. The FLC's output functions are represented in Figure 10. Designing membership functions makes use of the Gaussian curve. The fuzzy operator's input contains two or more relationship values derived from the input variables of the fuzzifier. Eight fuzzy subsets of the linguistic variables—five of which are used—are explained as follows:

(i) Negative error voltage big (NB)
(ii) Negative error voltage small (NS)
(iii) Positive error voltage big (PB)
(iv) Positive error voltage small (PS), and
(v) Zero error voltage (ZE)

FLC enables the system to adjust to varying conditions by changing the DC link voltage based on the reference voltage, the bus bar voltage, and the battery charge level. This variable represents the difference in voltage in the bus bar between the reference and actual voltages. The input variables are processed using the Mamdani fuzzy inference system, which then applies the proper control actions. The centroid method is used to defuzzify the output of the fuzzy inference system. The FLC uses this variation as an input. An optimistic mistake in the membership function of this variable could come from an excess supply if the actual voltage is larger than the reference voltage. The FLC determines the required changes for the DC link voltage by evaluating the input error voltage resulting from the voltage and battery charge variations. FLC is capable of adapting to

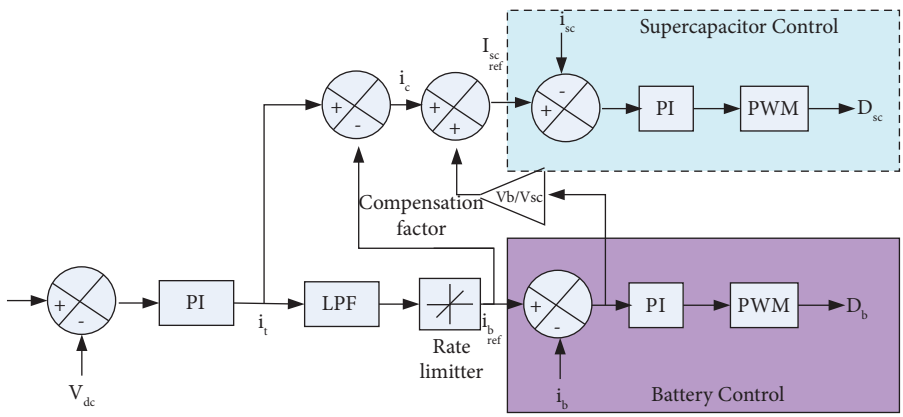

Figure 8: BC with traditional PI controller.

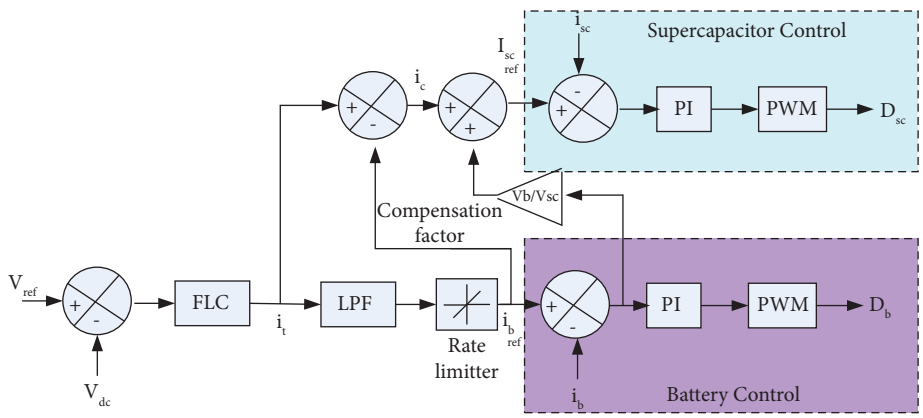

Figure 9: BC with FLC controller.

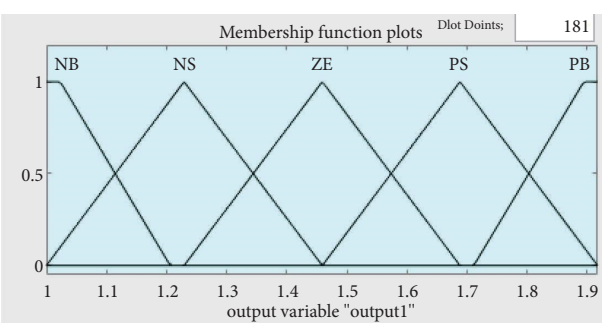

Figure 10: Membership function of FLC.

changes in voltage, making it helpful in dealing with dynamic load circumstances and system disruptions. The input variables are processed using the Mamdani fuzzy inference system, which then applies the proper control actions. The centroid technique is used to defuzzify the output of the fuzzy inference system.

4.3. SoC for SCs. The ESR of SC is considerably lower than that of batteries. They cannot conserve energy for an extended period as a result. The control logic prevents SC energy from the lowest allowable level by maintaining the SoC within the proper energy boundaries. When the SC's SoC falls below the required minimum, it gets charged by the battery at a set current. As indicated in Section 4, the buck or boost operation maintains the SoC of the SC within permitted limits. The SC current is regulated by an FLC. To govern the transfer mechanism, the controller was designed in the buck form. It is critical to note that if the HESS energy transfer mode is activated, the DC microgrid could get immediately disconnected from the HESS.

5. Results and Discussion

The results of two different cases employing the proposed method are presented in this section. To perform constant and variable irradiation with FLC, the simulation model was created in MATLAB/Simulink 2023a, and the system parameters are shown in Table 1. Figure 11 shows the simulation environment for the proposed methodology. The boost converter and PV array system are connected only in one direction. The following sections provide descriptions of the two operational situations for a step shift in load demand and PV output.

Table 1: System parameter.

Symbol	Parameters	Value
PV panel		
V_{oc}	Open circuit voltage	23 V
I_{sc}	Short circuit current	7 A
N_{cell}	Number of cells per module	120
P_m	Maximum power	200 W
N_{panel}	Number of panels	2
R_{sh}	Shunt resistance	10.30 Ω
R_{se}	Series resistance	0.009 Ω
Battery		
V_b	Battery voltage	45 V
Q	Battery capacity	50 Ah
R_{int}	Internal resistance	0.009 Ω
L_b	Inductance	10 mh
Supercapacitor		
V_{sc}	Supercapacitor voltage	48 V
T_{sc}	Operating temperature	25°C
N_{s_sc}	Number of series capacitors	4
N_{p_sc}	Number of parallel capacitors	6
L_s	Inductance	10 mH
R_L	Load resistance	5.2 Ω

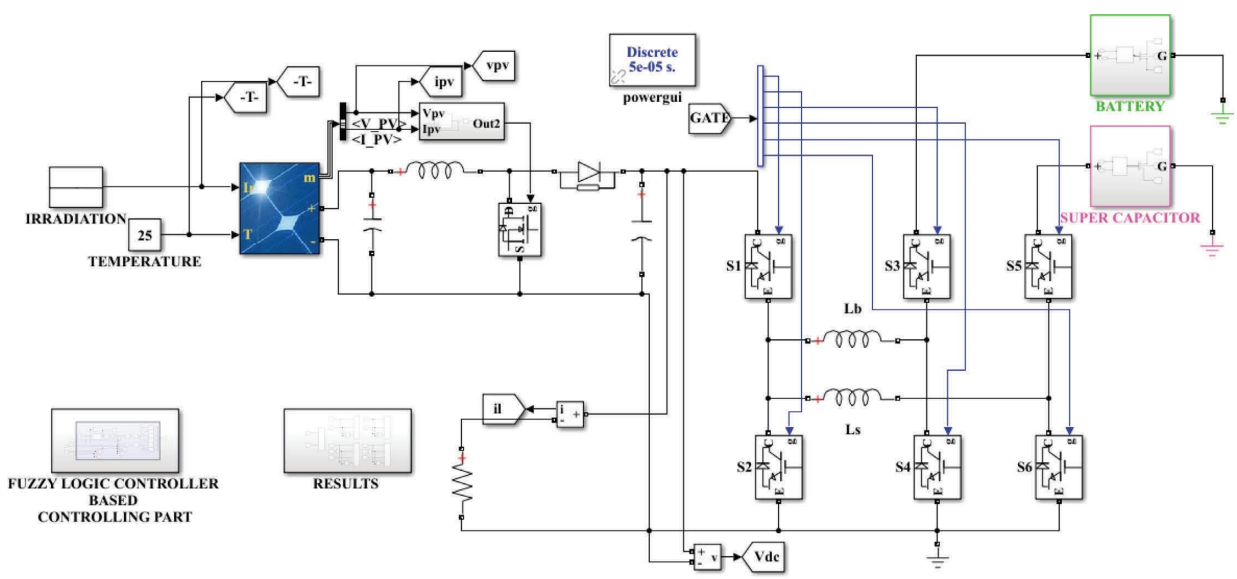

Figure 11: Simulation response of proposed system.

5.1. Case 1: Step Rise in Irradiation and Constant Temperature. Figure 12 illustrates the simulation behaviour of a step variation in irradiation and a constant temperature. The constant temperature is 25°C, and the step change variation is 1 second with 1000 w/m^2. Figure 13 depicts the panel voltage, current, and power simulation response. The power generated by the PV panel rises from 0 W to 200 W at $t = 0.1$ s due to environmental fluctuations. At $t = 0.1$ s, this PV causes the current to grow from 0 A to 6 A. Voltages, currents, and power fluctuated from 1 to 1.3 seconds due to transients. The panel is kept in constant condition for 1.3 seconds. Figure 14 exhibits the DC grid voltage and line current simulation response. The line current is kept at 2.4 A, and the grid voltage is kept at 55 V due to changes in irradiation. The transitory condition lasts between 1 and 1.3 seconds.

Figure 15 depicts the simulation response for battery voltage, current, SoC percentage, and battery power. After 1.3 seconds, the battery power is maintained at 3300 W. After 1.3 seconds, the battery voltage and current are still 40 V and 48 A, respectively, due to the step increase in irradiation. After 1.3 seconds, the battery's SoC % drops from 50 to 49.9 as a result of the load demand. Figure 16 illustrates the simulation response for SC voltage, current, SoC percentage, and battery power. DC grid voltage rises beyond 52 V. Then SC temporarily absorbs extra power until the battery can adjust the grid voltage up to 52 V. The SC and battery charge are in line with the power management plan to maintain the voltage level at 55 V. Due to the load requirement, the battery's SoC% marginally decreases after 1.3 seconds, with a value ranging from 98.5 to 98.3.

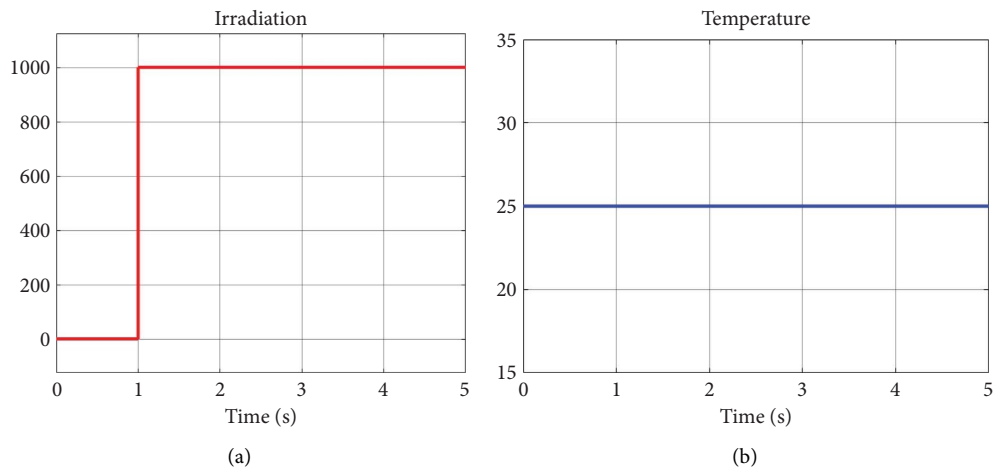

Figure 12: Simulation response of step change in irradiation and constant temperature.

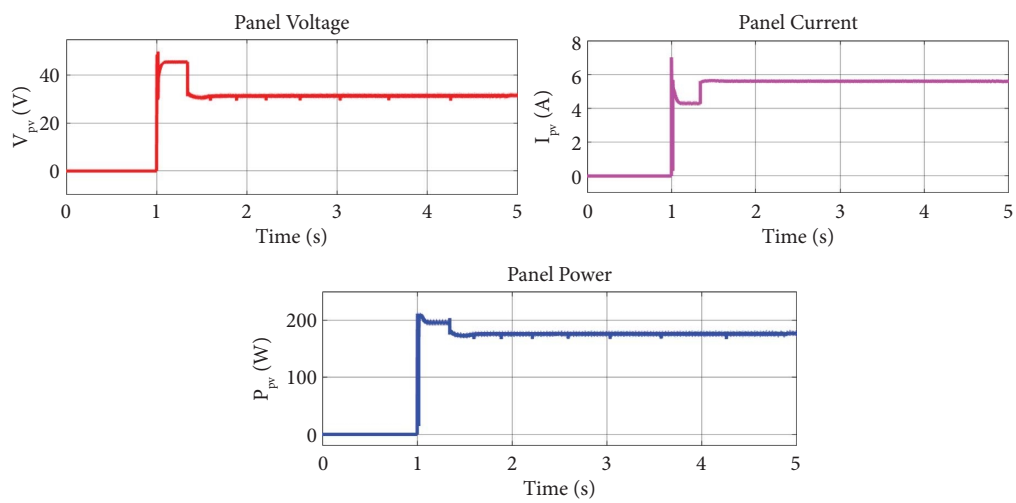

Figure 13: Response of panel voltage, current and power.

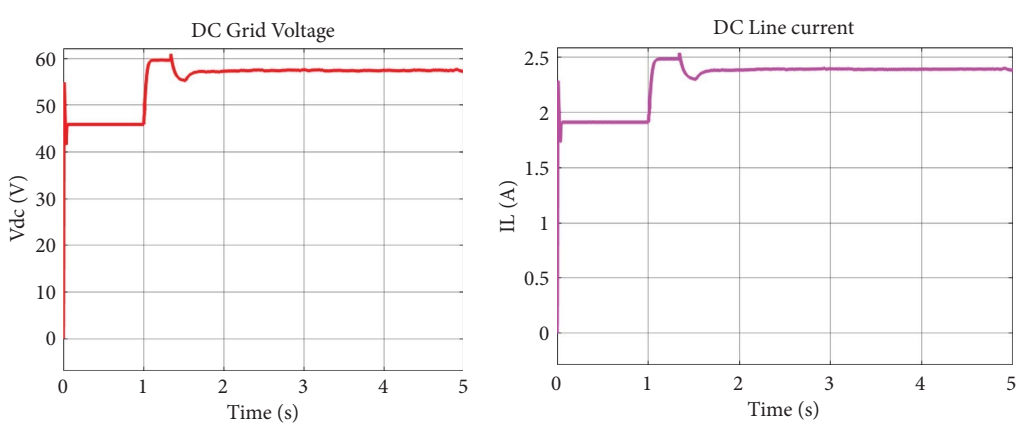

Figure 14: Response of DC grid voltage and line current.

5.2. Case 2: Variable Irradiation and Fixed Temperature. The simulated behaviour under variable irradiance and constant temperature is shown in Figure 17. The constant temperature is stated as 25°C, and the step change variation is given from 1000 w/m^2 to 0 at $t = 1$ second, and the step increase is from 0 to 1000 w/m^2 at 3 seconds. Figure 18 depicts the simulation response for panel voltage, current, and power. The power generated through the panel rises

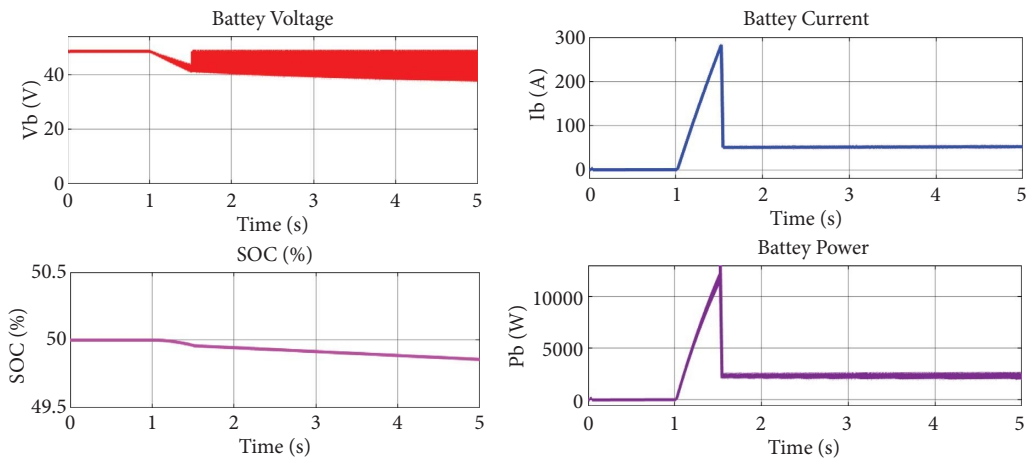

Figure 15: Simulation response of battery voltage, current, % of SoC, and battery power.

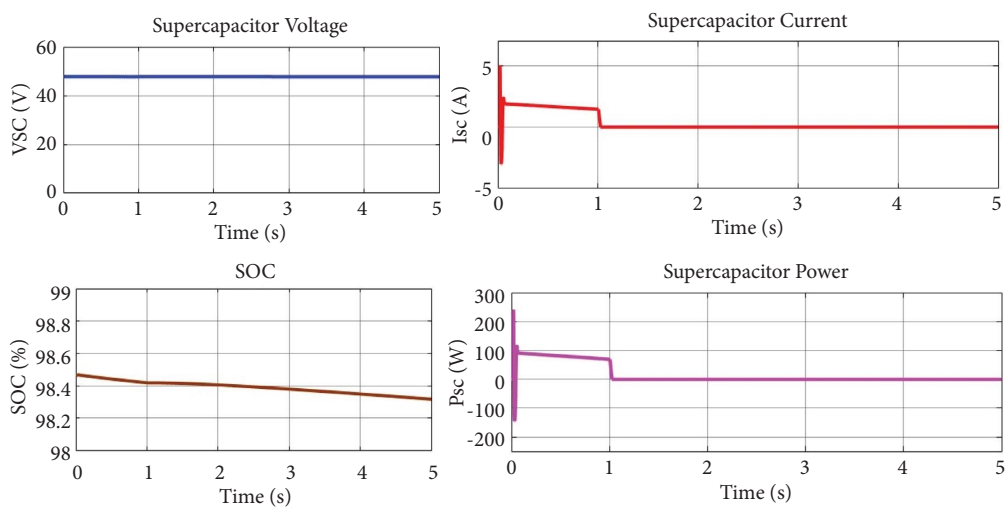

Figure 16: Simulation response of SC voltage, current, % of SoC, and battery power.

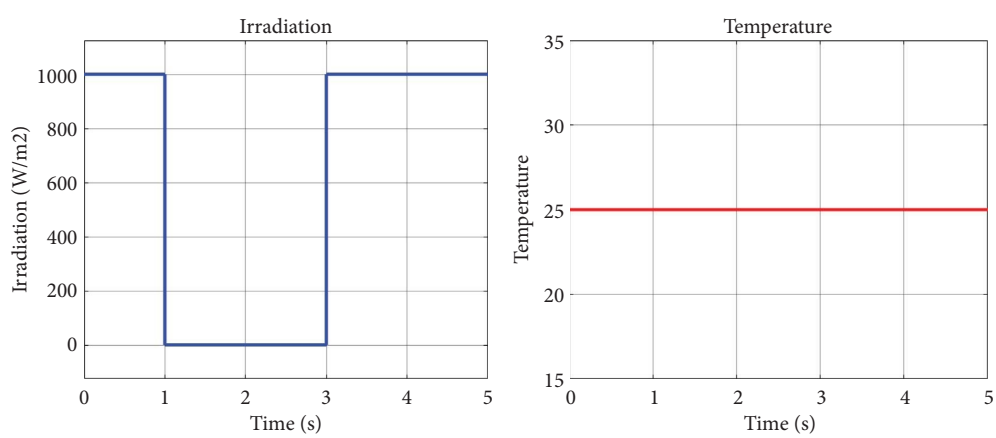

Figure 17: Simulation response of variable irradiation and temperature.

from 0 W to 100 W at $t = 3$ s as a consequence of environmental fluctuations. At $t = 3$ s, this PV causes the current to grow from 0 A to 6 A. Voltages, currents, and power fluctuated from 3 to 3.1 seconds due to transients. PV current steps down from 6 A to 0 A at $t = 1$ second due to the step drop in PV production. The panel is kept in constant condition after 3.1 seconds. Figure 19 exhibits the DC grid voltage and line current simulation responses. The line

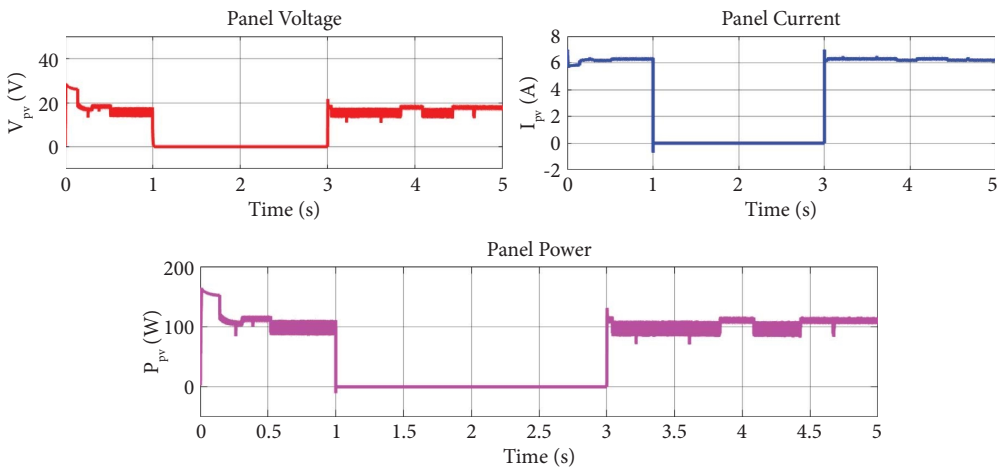

Figure 18: Simulation response of panel voltage, current, and power.

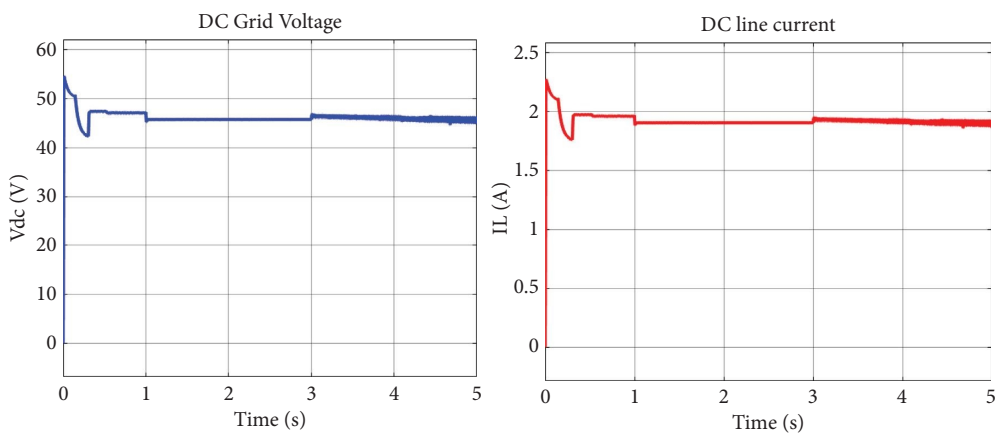

Figure 19: Simulation response of DC grid voltage and line current.

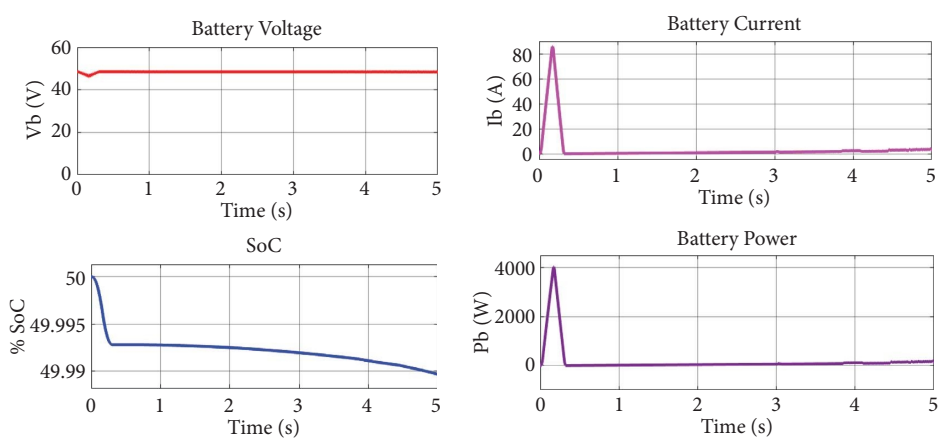

Figure 20: Simulation response of battery voltage, current, % of SoC, and battery power.

current is kept at 1.8 A, and the grid voltage is kept at 45 V due to changes in irradiation. The transitory condition lasts between 3 and 3.1 seconds. DC grid voltage drops as a result of the rapid drop in PV generation.

Figure 20 depicts the simulation response for battery voltage, current, SoC percentage, and battery power under variable irradiance state. After 0.3 seconds, the battery power is maintained at 3300 W. After 1.3 seconds, the battery voltage

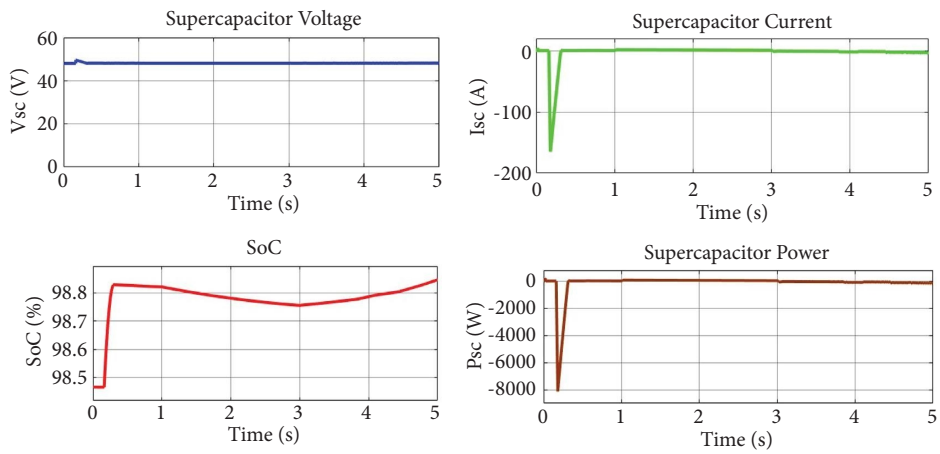

Figure 21: Simulation response of SC voltage, current, % of SoC, and battery Power.

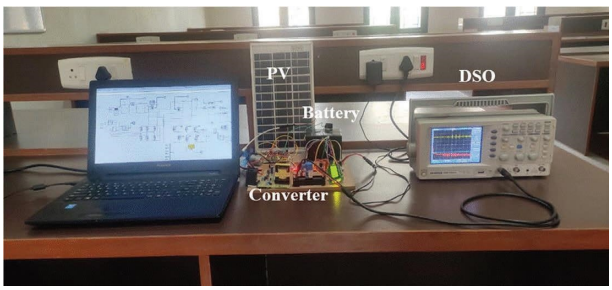

Figure 22: Experimental setup of proposed system.

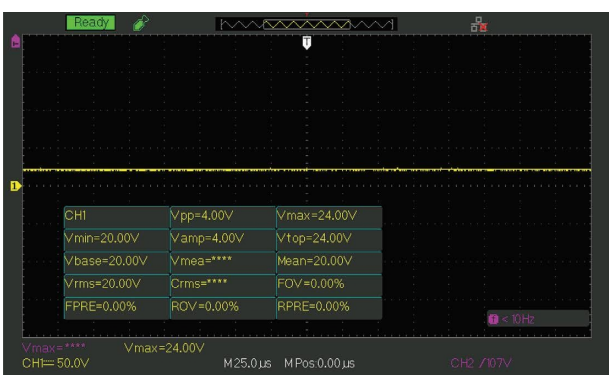

Figure 23: Experimental result of PV voltage under charging mode.

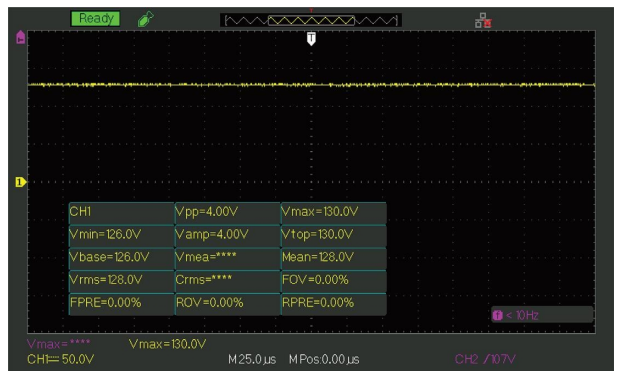

Figure 24: Experimental result of battery voltage under charging mode.

Figure 25: Switching pulses for the BC.

and current are still 40 V and 48 A, respectively, due to the step increase in irradiation. At 0.1 seconds, the battery's SoC % drops from 50 to 49.9 due to a change in the load demand. Figure 21 illustrates the simulation response for SC voltage, current, SoC percentage, and battery power. DC grid voltage rises beyond 45 V as PV power surpasses the load power needs. As soon as possible, SC temporarily absorbs extra power till the battery can adjust the grid voltage to 45 V. The batteries and SC recharge in line with the smart energy plan to maintain the voltage level at 45 V. Due to the load requirement, the battery's SoC % marginally decreases from 98.8 to 98.7 at $t = 1$ seconds. The HESS responds instantly, the SC provides the transient portion, and the battery provides the steady-state portion of power demand.

5.3. Experimental Setup. A hardware prototype for a standalone PV with HESS has been constructed in Figure 22. The Semikron switches are utilized to construct a DC-DC converter. A PV generator known as a regulated power supply (RPS) is used in this experiment. By controlling the current flowing from the RPS to the DC-DC boost converter,

the step change in input power is achieved. The HESS is powered by lead-acid batteries (17 Ah, 12 V). The dSPACE 1103 controller platform is used to implement the proposed control strategy. Under scenarios of constant irradiance and step changes in irradiance, the proposed system is evaluated. The step change in irradiance is used to test the proposed controller's capacity to handle rapid variations in peak load and production. The battery's SOC is kept within the appropriate safe operating ranges even during abrupt fluctuations in the PV panel voltage. (See Figure 23).

5.3.1. Case 1: Fixed Irradiation Mode. The effectiveness of the established controller is examined in the case of fixed radiation for DC voltage. Figure 24 depicts the appropriate waveform of PV generation under a fixed irradiation situation. The operational stability of the converter in maintaining voltage balance was evaluated by measuring the PV voltage at 20 V under the steady-state situation. Figure 25 illustrates the experimental battery voltage waveform under constant irradiation at a voltage of 40 V. It illustrates that the proposed bidirectional can continue to operate in charging mode while maintaining a constant DC voltage level.

Figure 26 illustrates the gate pulse sequence for the proposed convertor's active switches with a 62.04% duty cycle. The switch's switching voltage is 16.7 V. It illustrates that when the inductor is turned on, the current travelling through it grows linearly. Figure 25 shows the boost converter's inductive voltage waveform. With a duty cycle of 36.93% (1 Division = 5 V). The switching frequency of the obtained waveform is 18.2 KHz, and it provides 32 V. According to the results, when a MOSFET is turned on, input voltage Vin is provided across the inductor circuit, and the coil strives to grow in current as it stores energy. The results show that we can restore the DC link voltage more quickly by deflecting uncompensated energy from the battery pack to the controller.

5.3.2. Case 2: Step Increase in PV Generation. Figure 27 illustrates the experiment results for a step increase in the PV system. The PV voltage should be kept at 4.2 V when the load demand steps up. A step variation in load demand significantly impacts the DC link voltage. The HESS manages the system's abrupt power fluctuation. Figure 28 shows the experimental battery unit waveform in step-rising PV generating mode. With the proposed regulation, we could restore voltage faster and with minimum overshoot. The results demonstrate that the proposed method of control has excellent dynamical performance.

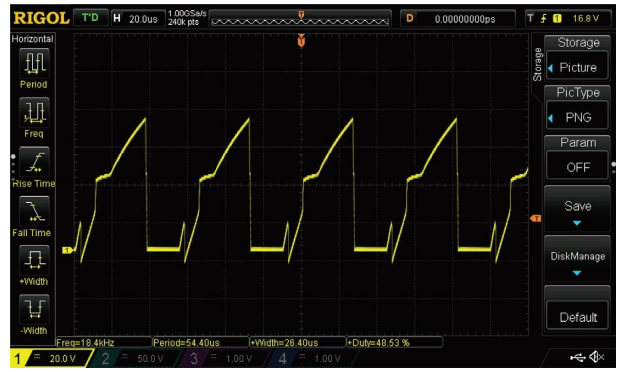

Figure 26: Experimental result of inductance voltage.

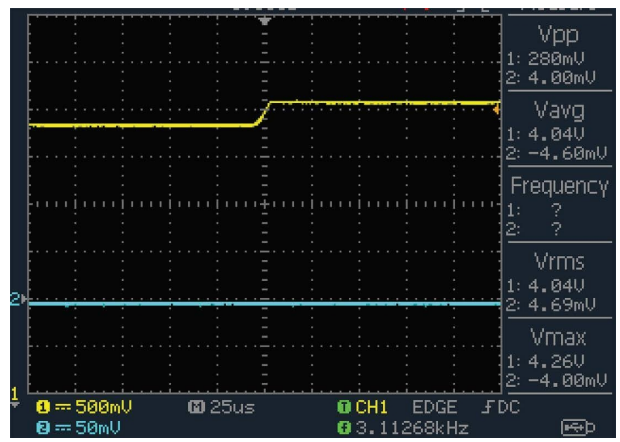

Figure 27: Experimental result of step rises in PV voltage.

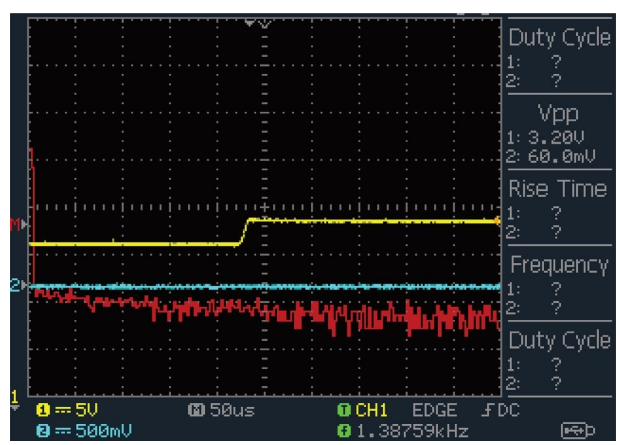

Figure 28: Experimental result of battery unit when step rises in PV voltage.

6. Discussion

For the proposed FLC technique's measuring performance, the overshoot and the settling time to recover the DC voltage link throughout a variation in load and production are measured. Comparing FLC to PI Controller, FLC is more resilient to manage such a broad range without needing constant adjustment. Table 2 compares the PI and proposed FLC strategies with two different scenarios. The proposed FLC responds two times quicker than a traditional controller. When sudden changes in irradiance occur, FLC brings the voltage back to the desired level in terms of transient responses like settling times and overshoot values. The system is made more flexible to parameter variation and robust to internal conflicts by the proposed control mechanism, which is intended such that the SC maintains the HESS till the batteries attain the steady-state configuration.

Table 2: Comparison of proposed FLC with conventional PI.

Time domain parameters	Scenarios			
	Step rise in PV		Step decrease in PV	
	Conventional PI [26]	Proposed FLC	Conventional PI [26]	Proposed FLC
Settling time (ms)	220	33	220	35
Maximum peak overshoot (Mp) in %	22.9%	19%	27%	22%

7. Conclusion and Future Work

The HESS controller was used to construct and simulate the controller for the multi-input BC. The performance of the designed controller for microgrid voltage regulation was evaluated in various circumstances. The controller stabilized the DC microgrid in contradiction of unfavorable effects from the source of PV production and different load types. It might use the built-in fast dynamics of the SC to quickly absorb microgrid transients. This proposed controller was crucial to the HESS's charging and discharging procedures.

Additionally, the HESS converter's mode of operation was shown to keep the SoC of the SC within a desirable range. The FLC makes sure that the BC is as efficiently controlled as possible and that it is managing the power divide between the DC supply and the load. During the step change in PV, the proposed FLC restores the voltage to the correct level regarding transient responsiveness, such as 33 ms settling times and 19% overshoot values. The findings demonstrate that the recommended FLC works better while employing SC and managing DC grid voltage. The proposed control approach delivers superior dynamic performance during a step variation in the PV system compared to the traditional control scheme. Based on the obtained results, the proposed system maintains load balance while achieving sufficient storage of energy and discharge.

From the perspective of future improvements, the proposed work can be expanded to include machine learning and deep neural networks (DNNs) to increase the converter's learning and control skills in HESS. Incorporate forecasting algorithms for solar irradiance and load estimates so that the neural network can make proactive energy management and storage decisions. It would also improve the neural network's identification of faults and irregularities in PV and storage systems, resulting in faster maintenance and increased reliability.

Data Availability

The data used to support the findings of this study are available from the corresponding author upon request.

Conflicts of Interest

The authors declare that there are no conflicts of interest regarding the publication of this paper.

Acknowledgments

The authors are thankful to the Deanship of Scientific Research at Najran University for funding this work under the Research Groups Funding program grant code (NU/RG/SERC/12/6).

References

[1] M. S. Nazir, Q. Wu, M. Li, and L. Zhang, "Symmetrical short circuit parameter differences of double fed induction generator and synchronous generator based wind turbine," *Indonesian Journal of Electrical Engineering and Computer Science*, vol. 6, no. 2, pp. 268–277, 2017.

[2] Irena, *Renewable Capacity Statistics 2019*, IRENA, Masdar City, UAE, 2019.

[3] A. Alzahrani, S. K. Ramu, G. Devarajan, I. Vairavasundaram, and S. Vairavasundaram, "A review on hydrogen-based hybrid microgrid system: topologies for hydrogen energy storage, integration, and energy management with solar and wind energy," *Energies*, vol. 15, no. 21, p. 7979, 2022.

[4] F. Díaz-González, C. Chillón-Antón, M. Llonch-Masachs et al., "A hybrid energy storage solution based on supercapacitors and batteries for the grid integration of utility scale photovoltaic plants," *Journal of Energy Storage*, vol. 51, Article ID 104446, 2022.

[5] M. S. Nazir, A. N. Abdalla, Y. Wang et al., "Optimization configuration of energy storage capacity based on the microgrid reliable output power," *Journal of Energy Storage*, vol. 32, Article ID 101866, 2020.

[6] M. S. Nazir, Y. Wang, A. J. Mahdi, X. Sun, C. Zhang, and A. N. Abdalla, "Improving the performance of doubly fed induction generator using fault tolerant control—a hierarchical approach," *Applied Sciences*, vol. 10, no. 3, p. 924, 2020.

[7] M. S. Nazir and W. Qi, "Impact of symmetrical short-circuit fault on doubly-fed induction generator controller," *International Journal of Electronics*, vol. 107, no. 12, pp. 2028–2043, 2020.

[8] M. R. Çorapsiz and H. Kahveci, "A study on Li-ion battery and supercapacitor design for hybrid energy storage systems," *Energy Storage*, vol. 5, no. 1, p. e386, 2023.

[9] H. Alafnan, X. Pei, M. Khedr et al., "The possibility of using superconducting magnetic energy storage/battery hybrid energy storage systems instead of generators as backup power sources for electric aircraft," *Sustainability*, vol. 15, no. 3, p. 1806, 2023.

[10] S. Kujur, H. M. Dubey, and S. R. Salkuti, "Demand response management of a residential microgrid using chaotic aquila optimization," *Sustainability*, vol. 15, no. 2, p. 1484, 2023.

[11] U. Manandhar, N. R. Tummuru, S. K. Kollimalla, A. Ukil, G. H. Beng, and K. Chaudhari, "Validation of faster joint

control strategy for battery-and supercapacitor-based energy storage system," *IEEE Transactions on Industrial Electronics*, vol. 65, no. 4, pp. 3286–3295, 2018.

[12] T. Mesbahi, P. Bartholomeüs, N. Rizoug, R. Sadoun, F. Khenfri, and P. L. Moigne, "Advanced model of hybrid energy storage system integrating lithium-ion battery and supercapacitor for electric vehicle applications," *IEEE Transactions on Industrial Electronics*, vol. 68, no. 5, pp. 3962–3972, 2021.

[13] S. K. Ramu, G. C. R. Irudayaraj, S. K. Paramasivam et al., "A simplified methodology for renewable energy integration and harmonic current reduction in hybrid micro grid," *Energy Sources, Part A: Recovery, Utilization, and Environmental Effects*, vol. 44, no. 4, pp. 8357–8379, 2022.

[14] W. Jing, C. Hung Lai, S. H. W. Wong, and M. L. D. Wong, "Battery-supercapacitor hybrid energy storage system in standalone DC microgrids: areview," *IET Renewable Power Generation*, vol. 11, no. 4, pp. 461–469, 2017.

[15] N. Lee, C. H. Nee, S. S. Yap et al., "Capacity sizing of embedded control battery–supercapacitor hybrid energy storage system," *Energies*, vol. 15, no. 10, p. 3783, 2022.

[16] Z. Song, J. Li, X. Han et al., "Multi-objective optimization of a semi-active battery/supercapacitor energy storage system for electric vehicles," *Applied Energy*, vol. 135, pp. 212–224, 2014.

[17] M. Bahloul and S. K. Khadem, "Impact of power sharing method on battery life extension in Hess for grid ancillary services," *IEEE Transactions on Energy Conversion*, vol. 34, no. 3, pp. 1317–1327, 2019.

[18] M. S. Nazir, A. N. Abdalla, H. Zhao et al., "Optimized economic operation of energy storage integration using improved gravitational search algorithm and dual stage optimization," *Journal of Energy Storage*, vol. 50, Article ID 104591, 2022.

[19] D. Bazargan, S. Filizadeh, and A. M. Gole, "Stability analysis of converter-connected battery energy storage systems in the grid," *IEEE Transactions on Sustainable Energy*, vol. 5, no. 4, pp. 1204–1212, 2014.

[20] N. Mukherjee and D. Strickland, "Control of cascaded DC–DC converter-based hybrid battery energy storage systems—Part I: stability issue," *IEEE Transactions on Industrial Electronics*, vol. 63, no. 4, pp. 2340–2349, 2015.

[21] B. A. Taye and N. B. D. Choudhury, "A new control method of hybrid energy storage system for DC microgrid application," *Energy Storage*, vol. 6, no. 1, 2024.

[22] T. Boonraksa, W. Pinthurat, P. Wongdet, P. Boonraksa, B. Marungsri, and B. Hredzak, "Optimal capacity and cost analysis of hybrid energy storage system in standalone DC microgrid," *IEEE Access*, vol. 11, pp. 65496–65506, 2023.

[23] J. Liu, Y. Hou, J. Guo, X. Liu, and J. Liu, "A cost-efficient virtual synchronous generator system based on coordinated photovoltaic and supercapacitor," *IEEE Transactions on Power Electronics*, vol. 38, no. 12, pp. 16219–16229, 2023.

[24] S. K. Kollimalla, A. Ukil, H. B. Gooi, U. Manandhar, and N. R. Tummuru, "Optimization of charge/discharge rates of a battery using a two-stage rate-limit control," *IEEE Transactions on Sustainable Energy*, vol. 8, no. 2, pp. 516–529, 2017.

[25] K. K. Rout, D. P. Mishra, S. Mishra, S. Patra, and S. R. Salkuti, "Perturb and observe maximum power point tracking approach for microgrid linked photovoltaic system," *Indonesian Journal of Electrical Engineering and Computer Science*, vol. 29, no. 2, pp. 635–643, 2023.

[26] Q. Xu, J. Xiao, P. Wang, X. Pan, and C. Wen, "A decentralized control strategy for autonomous transient power sharing and state-of-charge recovery in hybrid energy storage systems," *IEEE Transactions on Sustainable Energy*, vol. 8, no. 4, pp. 1443–1452, 2017.

[27] Z. Yi, W. Dong, and A. H. Etemadi, "A unified control and power management scheme for PV-battery-based hybrid microgrids for both grid-connected and islanded modes," *IEEE Transactions on Smart Grid*, vol. 9, no. 6, pp. 5975–5985, 2018.

[28] R. S. Kumar, L. G. C. Raj, and J. Abarna, "Analysis of fuzzy logic based fault detection for three phase induction motor drive system," in *Proceedings of the 2018 4th International Conference on Electrical Energy Systems (ICEES)*, pp. 700–705, IEEE, Chennai, India, February 2018.

[29] S. Punna, S. Banka, and S. R. Salkuti, "Optimal energy management scheme of battery supercapacitor-based bidirectional converter for DC microgrid applications," *Information*, vol. 13, no. 7, p. 350, 2022.

[30] S. Choudhury and N. Khandelwal, "A novel weighted superposition attraction algorithm-based optimization approach for state of charge and power management of an islanded system with battery and supercapacitor-based hybrid energy storage system," *IETE Journal of Research*, vol. 69, no. 2, pp. 825–838, 2023.

[31] O. Tremblay, L.-A. Dessaint, and A.-I. Dekkiche, "A generic battery model for the dynamic simulation of Hybrid Electric Vehicles," in *Proceedings of the 2007 IEEE Vehicle Power and Propulsion Conference*, Arlington, TX, USA, September 2007.

[32] K. B. Oldham, "A Gouy–Chapman–Stern model of the double layer at a (metal)/(ionic liquid) interface," *Journal of Electroanalytical Chemistry*, vol. 613, no. 2, pp. 131–138, 2008.

[33] T. B. Nkwanyana, M. W. Siti, Z. Wang, I. Toudjeu, N. T. Mbungu, and W. Mulumba, "An assessment of hybrid-energy storage systems in the renewable environments," *Journal of Energy Storage*, vol. 72, Article ID 108307, 2023.

[34] S. Punna, R. Mailugundla, and S. R. Salkuti, "Design, analysis and implementation of bidirectional DC–DC converters for Hess in DC microgrid applications," *Smart Cities*, vol. 5, no. 2, pp. 433–454, 2022.

[35] A. Hintz, U. R. Prasanna, and K. Rajashekara, "Novel modular multiple-input bidirectional DC–DC power converter (MIPC) for HEV/FCV application," *IEEE Transactions on Industrial Electronics*, vol. 62, no. 5, pp. 3163–3172, 2015.

[36] B. Wang, X. Zhang, U. Manandhar, H. B. Gooi, Y. Liu, and X. Tan, "Bidirectional three-level cascaded converter with deadbeat control for HESS in solar-assisted electric vehicles," *IEEE Transactions on Transportation Electrification*, vol. 5, no. 4, pp. 1190–1201, 2019.

[37] S. Punna, U. B. Manthati, and A. Chirayarukil Raveendran, "Modeling, analysis, and design of novel control scheme for two-input bidirectional DC-DC converter for HESS in DC microgrid applications," *International Transactions on Electrical Energy Systems*, vol. 31, no. 10, Article ID e12774, 2021.

[38] R. R. Deshmukh, M. S. Ballal, and H. M. Suryawanshi, "A fuzzy logic based supervisory control for power management in multibus DC microgrid," *IEEE Transactions on Industry Applications*, vol. 56, no. 6, pp. 6174–6185, 2020.